# Development of Görtler vortices in a serpentine diffuser

**By A. Nekkanti, R. Agrawal, S. T. Bose AND P. Moin**

This work investigates the flow through a serpentine diffuser using wall-modeled large-eddy simulations (WMLESs). Following Agrawal *et al.* (2025), who demonstrated that WMLES with the charLES flow solver can accurately predict pressure recovery and azimuthal flow distortion within experimental error bounds, we conduct simulations at three Mach numbers (at the duct exit plane), $Ma_{\mathrm{AIP}} = 0.36, 0.46$ and $0.54$. The serpentine diffuser features two longitudinal bends where a pair of counter-rotating streamwise vortices are generated. We focus on characterizing these vortices and their influence on azimuthal flow distortion and pressure recovery loss at the aerodynamic interface plane (AIP), which can limit aerodynamic efficiency. The adverse pressure gradient at the bends induces flow separation, while centrifugal forces generate a pair of counter-rotating Görtler vortices. As the axial cross-section of the diffuser transitions from elliptical to circular, these vortices move toward the centerline along the spanwise direction, ejecting low-momentum fluid from near the wall into the core and thereby causing azimuthal distortion and a reduction in pressure recovery. Statistical quadrant analysis shows that ejection events dominate near the onset of the Görtler vortices, while sweep events become more prevalent downstream. Conditional quadrant analysis further reveals that ejection events correspond to maximum azimuthal distortion and pressure loss, whereas sweep events tend to minimize these effects.

## 1. Introduction

Blended wing body configurations are a promising design for future military aircraft, integrating engines within the fuselage to improve efficiency. These require compact inlets, including serpentine ducts (Brear *et al.* 2004; Winkler & Davis 2017) whose high-curvature bends generate large-scale vortices, shock waves and flow separation (Ng *et al.* 2008). Such typically unsteady flow features can increase turbine load, reduce stall margin and, in severe cases, lead to engine failure. In particular, non-uniform inflow conditions at the inlet exit can degrade aerodynamic performance, diminish engine operability and elevate mechanical stress on turbine blades (Triantafyllou *et al.* 2015).

Flow through curved ducts, such as curved channels, 90° bend pipes and S-shaped diffusers, experiences radial pressure gradients and centrifugal forces that induces secondary flows along the walls and may lead to flow separation, leading to increased pressure losses, flow distortion and non-uniform pressure distribution at the AIP (Wenzel & Blaha 1977). Counter-rotating vortices are formed inside the duct, downstream of the bends. These vortices, reminiscent of Görtler vortices and sometimes referred to as Dean vortices (Dean 1927, 1928), entrain the boundary-layer fluid into the core, degrade pressure uniformity and reduce pressure recovery (Brear *et al.* 2004; Ng *et al.* 2008). Recent experiments have shown that pressure distortion is strongly influenced by Mach number, with recent experiments (Huang *et al.* 2024; Stratton *et al.* 2025) reporting a substantial 5.5%

increase in pressure loss as $Ma_{\mathrm{AIP}}$ increases from 0.3 to 0.55. In addition to the mean total pressure distortions, the unsteady flows within serpentine diffusers also exhibit large peak dynamic distortions (Zachos *et al.* 2016; MacManus *et al.* 2017), which may trigger compressor instabilities even when mean levels remain within acceptable limits. Further, it is often difficult in experiments of serpentine ducts to analyze three-dimensional flow structure upstream of the AIP non-intrusively. To this end, this work examines the spatial development of counter-rotating vortices, their role in generating mean distortion and the sensitivity of these vortices to Mach number for the flow inside a serpentine duct (SD-2), studied experimentally by Burrows *et al.* (2021).

Numerous experimental campaigns (for example: Brear *et al.* 2004; Ng *et al.* 2008; Harrison *et al.* 2013) have previously studied the flow through serpentine diffusers. However, only a few numerical studies have been conducted to physically characterize the mechanism of flow distortion. Previously, for the SD-2 duct, Lakebrink & Mani (2018) showed that Reynolds-averaged Navier-Stokes (RANS) models overpredict mean flow recovery, while detached eddy simulations (DESs) provide relatively more accurate results, their predictions still deteriorate with increasing Mach number. Similarly, Lakebrink *et al.* (2019) and Stahl *et al.* (2023) reported overpredictions of pressure recovery at the exit plane. Recently, Agrawal *et al.* (2025) performed wall-modeled large eddy simulations of the SD-2 diffuser using both the dynamic Smagorinsky (Moin *et al.* 1991) and equilibrium wall models (Cabot & Moin 2000), as well as the more recent dynamic tensor-coefficient Smagorinsky subgrid-scale (Agrawal *et al.* 2022) and sensor-aided non-equilibrium wall models (Agrawal *et al.* 2024*a*). They demonstrated that while both approaches provide good predictions, the latter one in particular accurately captures pressure recovery and azimuthal flow distortion within the experimental error bounds. This brief builds on their work and investigates the flow physics underlying azimuthal distortion for three different mass flow rates.

The rest of this brief is organized as follows: Section 2 provides a brief overview of the governing equations and computational solver, results are presented in Section 3, and concluding remarks are offered in Section 4.

## 2. Governing equations and computational solver

In this work, we utilize the charLES flow solver to perform large eddy simulations. CharLES is an explicit, unstructured, finite-volume solver which solves the filtered compressible Navier-Stokes equations (see below) and is second-order accurate in space and third-order accurate in time. For further details on the solver and relevant validation studies, the reader is referred to Brès *et al.* (2018), Goc *et al.* (2023) and Agrawal *et al.* (2024*b*, 2025). The resulting system of equations is

$$\frac{\partial \bar{\rho}}{\partial t} + \frac{\partial (\bar{\rho}\,\tilde{u}_j)}{\partial x_j} = 0, \tag{2.1}$$

$$\frac{\partial (\bar{\rho}\,\tilde{u}_i)}{\partial t} + \frac{\partial (\bar{\rho}\tilde{u}_i\tilde{u}_j)}{\partial x_j} = -\frac{\partial \bar{p}}{\partial x_j} + \frac{\partial \tilde{\tau}_{ij}}{\partial x_j} - \frac{\partial \tilde{\tau}_{ij}^{\mathrm{sgs}}}{\partial x_j}, \tag{2.2}$$

$$\frac{\partial \bar{E}}{\partial t} + \frac{\partial (\bar{E}\tilde{u}_j)}{\partial x_j} = -\frac{\partial \bar{p}\tilde{u}_j}{\partial x_j} + \frac{\partial \tilde{\tau}_{ij}\tilde{u}_i}{\partial x_j} - \frac{\partial \tilde{\tau}_{ij}^{\mathrm{sgs}}\tilde{u}_i}{\partial x_j} - \frac{\partial \tilde{Q}_{ij}^{\mathrm{sgs}}}{\partial x_j} + \frac{\partial}{\partial x_j}\left(\kappa \frac{\partial \bar{T}}{\partial x_j}\right), \tag{2.3}$$

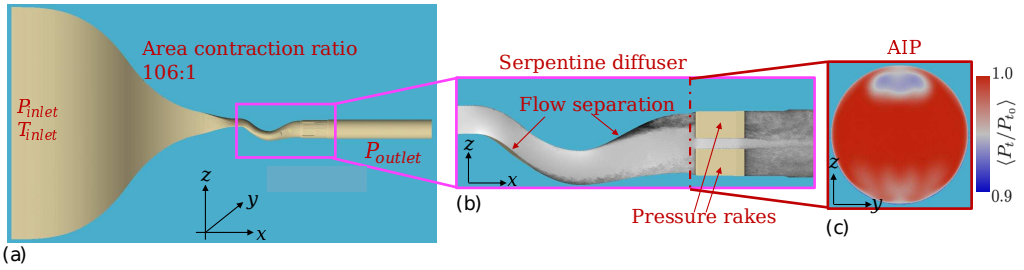


FIGURE 1. (a) Schematic of the computational setup, which includes a contracting inlet of area ratio 106:1, leading to the test section of the serpentine diffuser followed by a cylindrical section. (b) Streamwise velocity shown on $xz$-plane. (c) Total pressure at the AIP. Panel (a) was reproduced from Agrawal *et al.* (2025) with permission.

where $\bar{(\cdot)}$ and $\tilde{(\cdot)}$ denote the filtered and Favre-averaged quantities, respectively. Here, $u_i$ represent the $i$-th component of velocity, $p$ the pressure, $\rho$ the density, $E$ the total energy and $T$ the temperature, while $\tau_{i,j}$ and $\tau_{i,j}^{\text{sgs}}$ are the viscous and subgrid stresses, respectively. In this brief, we invoke the dynamic Smagorinsky model of Moin *et al.* (1991) for closing the subgrid-scale model. A constant molecular Prandtl number ($Pr = 0.7$) is used to compute the thermal conductivity ($\kappa$), while the subgrid heat flux is computed using a constant turbulent Prandtl number approximation ($Pr_t = 0.9$). The equilibrium wall model closes the wall shear stress and heat flux at the solid walls of the diffuser.

Recently, Agrawal *et al.* (2025) validated the flow through the SD-2 duct at three different Mach numbers: $Ma_{\text{AIP}} = 0.36, 0.46$ and $0.54$. They demonstrated that a mesh containing three billion grid points is adequate to capture the pressure recovery and flow distortion at the AIP within experimental uncertainty bounds for all flow rates. Following their work, we perform three WMLESs at mass flow rates of 1.61, 1.95 and 2.27 kg/s, on the 'L7' grid (see Agrawal *et al.* 2025), which contains three billion control volumes.

## 3. Results

The computational setup, shown in Figure 1(a), consists of a bellmouth contraction inlet with an area ratio of 106:1 that accelerates the flow into the diffuser (test section). Downstream of the diffuser is a cylindrical section that houses the pressure probe rakes and acts as the flow outlet.

First, we present the results at the lowest Mach number, $Ma_{AIP} = 0.36$; and the effects of Mach number are discussed later. Figure 1(b) illustrates the instantaneous streamwise velocity contours in the $xz$-plane; the contours reveal that the flow separation occurs at the bends of the diffuser, at $x/D_{AIP} \approx -3.00$ and $x/D_{AIP} \approx -1.60$, respectively. The adverse pressure gradients, combined with the curvature effects at these bends, lead to separation, which consequently causes azimuthal flow distortion at the AIP [see Figure 1(c)]. The flow separation induced by the second bend along the upper wall exerts a stronger influence, likely due to its spatial proximity, on the distortion at the AIP, manifested by the blue contours in Figure 1(c). Flow separation along the bottom wall also causes distortion and a loss of total pressure, albeit to a lesser extent.

Next, we characterize the streamwise flow and the azimuthal distortion at $Ma_{AIP} \approx 0.36$ condition in Figures 2 and 3. Figure 2 presents the mean streamwise vorticity at several axial cross-sections, $-1.18 \leq x/D_{AIP} \leq 0.0$, spanning the separated region close

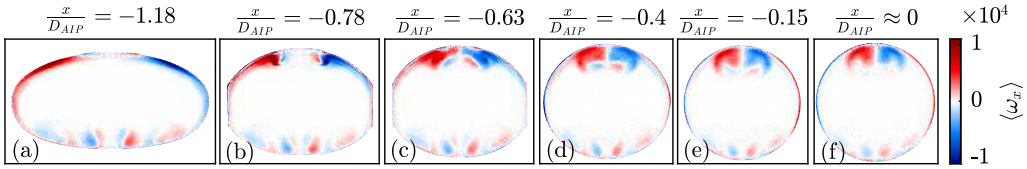


FIGURE 2. Mean streamwise vorticity at different axial planes for the flow inside the SD-2 diffuser at $Ma_{AIP} \approx 0.36$ conditions. The locations are (a) $x/D_{AIP} = -1.18$, (b) $x/D_{AIP} = -0.78$, (c) $x/D_{AIP} = -0.63$, (d) $x/D_{AIP} = -0.4$, (e) $x/D_{AIP} = -0.15$ and (f) $x/D_{AIP} \approx 0$ (AIP).

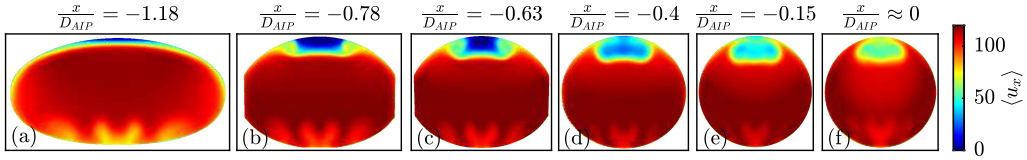


FIGURE 3. Mean streamwise velocity at different axial planes for the flow inside the SD-2 diffuser at $Ma_{AIP} \approx 0.36$ conditions. The locations are (a) $x/D_{AIP} = -1.18$, (b) $x/D_{AIP} = -0.78$, (c) $x/D_{AIP} = -0.63$, (d) $x/D_{AIP} = -0.4$, (e) $x/D_{AIP} = -0.15$ and (f) $x/D_{AIP} \approx 0$ (AIP).

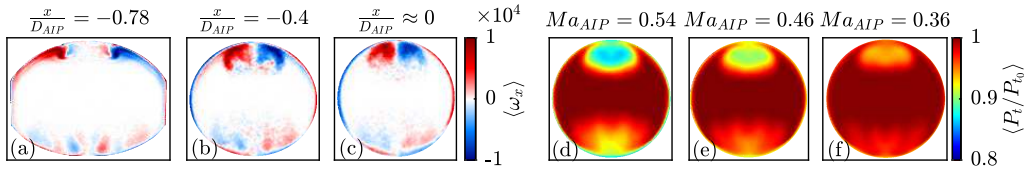


FIGURE 4. Mean streamwise vorticity at different axial planes for $Ma_{\mathrm{AIP}} = 0.54$ flow inside the SD-2 diffuser: (a) $x/D_{AIP} = -0.78$; (b) $x/D_{AIP} = -0.4$; (c) $x/D_{AIP} = 0$ (AIP). Total pressure at the AIP for different Mach number conditions: (d) $Ma_{\mathrm{AIP}} = 0.54$; (e) $Ma_{\mathrm{AIP}} = 0.46$; (f) $Ma_{\mathrm{AIP}} = 0.36$.

to the second bend leading up to the AIP. The vorticity contours demonstrate the presence of counter-rotating vortices along the upper wall, which develop as the boundary layer separates. These vortices, known as Görtler vortices, arise from radial pressure gradients induced by wall curvature. As the flow evolves downstream, the counter-rotating vortices move toward the centerline ($y/D_{AIP} = 0$) and into the core region. The vortices appear to be quasi-developed by $x/D_{AIP} = -0.15$, beyond which their spatial structure remains nearly identical. Additionally, pairs of counter-rotating vortices of lower amplitude are observed along the lower wall, likely originating from the boundary-layer separation induced by the first bend. Figure 3 presents the mean streamwise velocity at the same cross-sectional planes. At $x/D_{AIP} = -1.18$, a region of low streamwise velocity is observed along the top wall, which localizes closer to the centerline downstream. This low-momentum region lies between the counter-rotating vortices, as evidenced, for example, in Figures 2(b) and 3(b). Its emergence is consistent with the detachment of the boundary layer. This region is subsequently advected from the near-wall region into the core by the counter-rotating vortices. At the AIP, the low-momentum region coincides with the area of total pressure loss, which is expected because the reduced velocity lowers the total pressure. A similar behavior is observed along the bottom wall. Overall, these figures demonstrate that the Görtler vortices are present at the same locations at those of flow distortion and diminished recovery at the AIP.

To examine the effects of Mach number on the location and extent of these streamwise vortices, in Figure 4(a–c) we examine the mean streamwise vorticity and velocity at

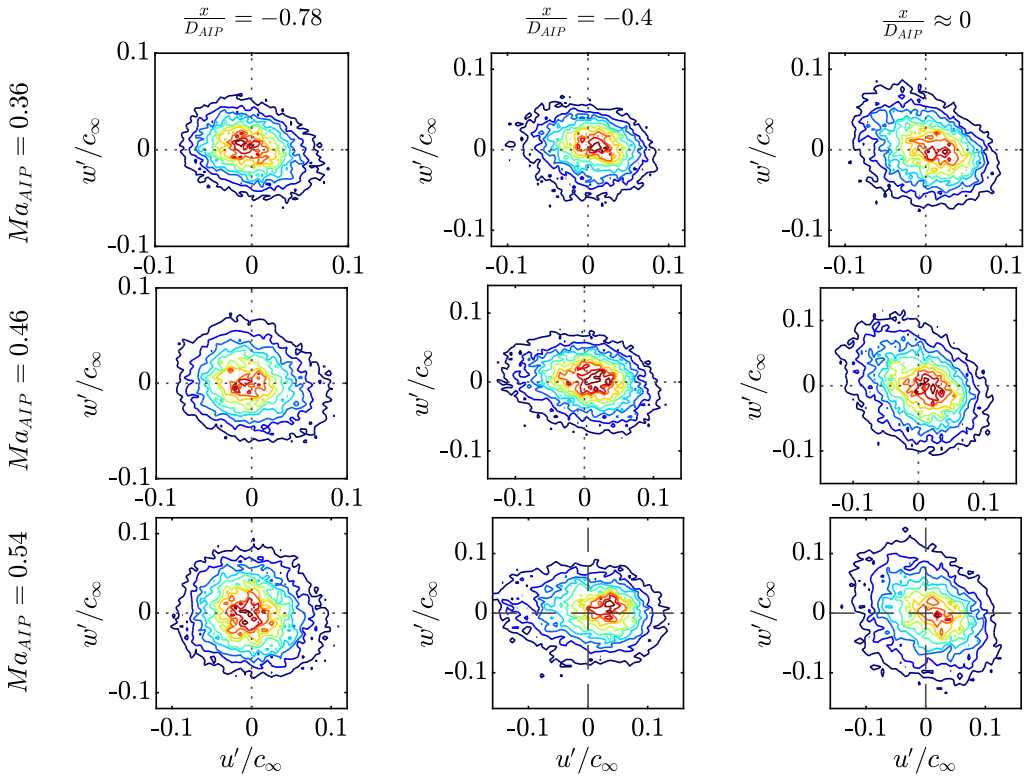


FIGURE 5. Joint probability density functions (JPDFs) of $u'$–$w'$ at different locations for varying Mach numbers. The Mach numbers $Ma_{\mathrm{AIP}} = 0.36, 0.46$ and 0.54 are shown in the top, middle, and bottom rows, respectively. The left, center and right columns correspond to axial locations $x/D_{AIP} = -0.78, -0.4$ and 0.0. Each plot is computed at the spatial location near the center of the vortex at the corresponding axial position.

$Ma_{\mathrm{AIP}} = 0.54$. Qualitatively, the spatial features of the streamwise vortices are identical to those observed at the lowest Mach number; however, at the increased Mach number, the vorticity amplitudes are higher. Figure 4(d–f) presents the total pressure at the AIP across the Mach number range; At the higher Mach numbers, the azimuthal distortion is larger and is localized near the region of Görtler vortices. Qualitatively, the azimuthal distortion patterns are of similar extent across the Mach numbers, which may suggest that while the Mach number amplifies the distortion, the underlying vortex dynamics are similar.

We recall that Figures 2 and 3 suggested that along the spatial extent of the AIP, the low-momentum fluid gets advected from the near-wall region toward the core. To gain further insight into this process, we perform a quadrant analysis of the AIP data. This analysis decomposes Reynolds shear stress ($-u'w'$, where $u'$ and $w'$ are the streamwise and wall-normal velocity fluctuations, respectively) into four quadrants: Q1, Q2, Q3 and Q4. In quadrant Q1, $u' > 0$ and $w' > 0$; in Q2, $u' < 0$ and $w' > 0$; in Q3, $u' < 0$ and $w' < 0$; and in Q4, $u' > 0$ and $w' < 0$. The Q2 and Q4 motions correspond to ejection and sweep events, respectively, whereas Q1 and Q3 represent outward and inward interactions (Corino & Brodkey 1969; Wallace *et al.* 1972). Figure 5 shows the joint probability distribution functions (JPDFs), $J(u', w')$, for the three Mach numbers at three axial

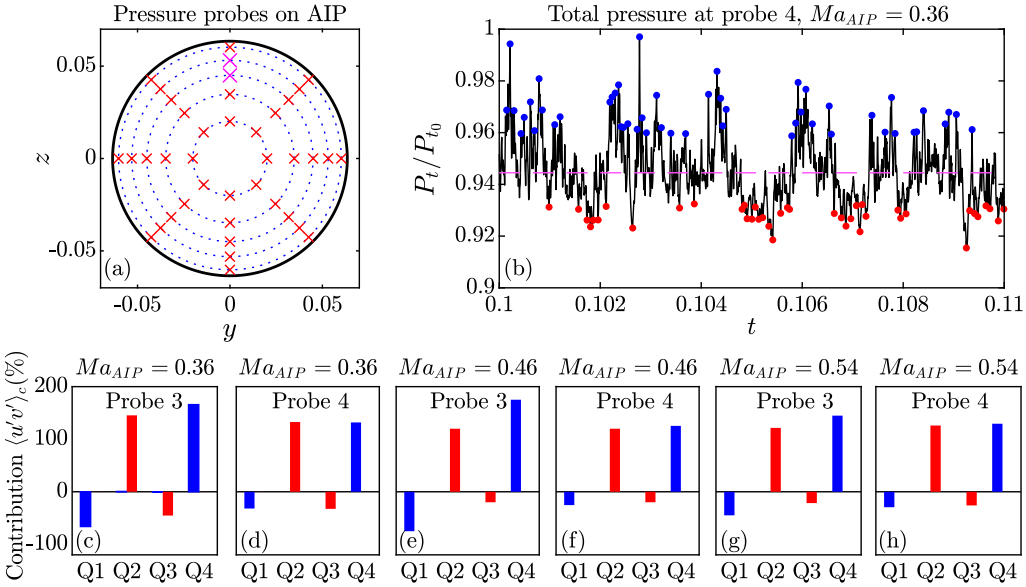


FIGURE 6. (a) Pressure probes distribution on the AIP, where $y$ and $z$ correspond to the spanwise and the vertical directions, respectively. (b) Time history of total pressure at Probe 4 ($x/D_{AIP} = 0$, $y/D_{AIP} = 0$, $z/D_{AIP} = 0.4$). A representative time interval is shown with local maxima and minima denoted by blue and red circles, respectively. Panels (c)-(h) show the percentage contribution of quadrant events Q1, Q2, Q3 and Q4 to Reynolds shear stress conditioned on the local maxima and minima of total pressure for $Ma_{\mathrm{AIP}} = 0.36, 0.46$ and $0.54$ at Probe 3 ($x/D_{AIP} = 0$, $y/D_{AIP} = 0$, $z/D_{AIP} = 0.35$) and Probe 4.

locations $x/D_{AIP} = -0.78$, $-0.4$ and $0.0$. Across all Mach numbers, the JPDFs exhibit an elliptical shape tilted toward the Q2 and Q4 quadrants. At $x/D_{AIP} = -0.78$, the JPDF is inclined toward Q2, indicating a strong correlation between negative streamwise fluctuations and positive vertical velocity fluctuations, which is physically consistent with dominant ejection events. Downstream, at $x/D_{AIP} = 0$, the JPDF is more inclined toward the Q4 quadrant, implying enhanced sweep activity. Across the Mach number range, the distributions widen slightly, reflecting stronger velocity fluctuations at the higher Mach number. However, the overall trend remains robust to the Mach number: Ejection events dominate near the onset of counter-rotating streamwise vortices, whereas sweep events dominate farther downstream.

Next, we relate the contribution of these quadrant events to the local maxima and minima of total pressure at the AIP, particularly along the centerspan region, on the top wall. For reference, Figure 6(a) presents the distribution of 40 dynamic pressure probes at the AIP. The probes positioned along $y/D_{AIP} = 0$ and $z/D_{AIP} > 0$ are located within the region of intense pressure losses, with the third and fourth probes (marked by $\times$ in magenta) placed closest to the point of maximum total pressure loss. The temporal history of the total pressure at the fourth probe for $Ma_{\mathrm{AIP}} = 0.36$ flow is shown in Figure 6(b) (for visual clarity, only a brief representative interval is presented). The mean total pressure at this probe is denoted by the dashed magenta line, while the local maxima and minima of the time series are marked by blue and red circles, respectively. Here, we consider the 500 most prominent maxima and minima identified over the time history. The local minima are indicative of instances of high pressure losses and vice versa. The conditional averages of the Reynolds shear stresses over the instances of the local

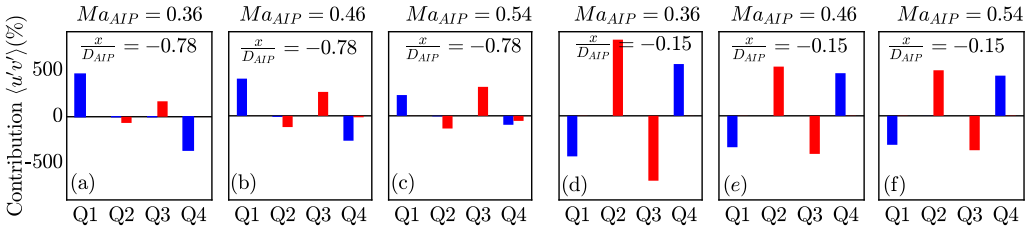


FIGURE 7. Percentage contribution of quadrant events Q1, Q2, Q3, and Q4 to Reynolds shear stress conditioned on the local maxima (blue) and minima (red) of total pressure: (a) $x/D_{AIP} = -0.78, Ma_{\text{AIP}} = 0.36$, (b) $x/D_{AIP} = -0.78, Ma_{\text{AIP}} = 0.46$, (c) $x/D_{AIP} = -0.78, Ma_{\text{AIP}} = 0.54$, (d) $x/D_{AIP} = -0.15, Ma_{\text{AIP}} = 0.36$, (e) $x/D_{AIP} = -0.15, Ma_{\text{AIP}} = 0.46$ and (f) $x/D_{AIP} = -0.15, Ma_{\text{AIP}} = 0.54$.

maxima and the minima are approximately 7.4 and 5.2 times larger than the averaged Reynolds shear stresses, respectively. This indicates that both the instances of maximum and minimum pressure losses are consistent with bursts of Reynolds shear stress.

The contributions of the four quadrant events (of the Reynolds shear stress) at the time instances corresponding to the local maxima and minima of total pressure are presented in Figure 6(c–h) for all three Mach numbers and on probes 3 and 4. Events conditioned on local maxima and minima are indicated in blue and red, respectively. The contributions of all four events sum to 100%. If a particular event exceeds 100%, it indicates that the other events contribute negatively, opposing its effect. A common trend is observed across both probes and all Mach numbers: Only Q2 and Q3 events contribute during intense pressure losses, whereas Q1 and Q4 events contribute to instances of higher pressure recovery. This further supports the conjecture that the ejection events drive the loss of total pressure (which also enhances azimuthal distortion), whereas the sweep events are associated with pressure gains (and reduce azimuthal distortions). The inward and outward interactions contribute negatively to the Reynolds shear stress, indicating that they counteract the effects of the ejection and sweep events during maximum and minimum azimuthal distortions. These trends are consistent across all Mach numbers, further suggesting that the same mechanism governs the flow behavior for the range of Mach numbers considered.

We now attempt to relate the total pressure fluctuations at the AIP with the Reynolds stress fluctuations upstream of the AIP to connect the flow dynamics across the duct. To that end, Figure 7 shows the conditional quadrant analysis for two upstream locations, $(x/D_{AIP}, y/D_{AIP}, z/D_{AIP}) = (-0.78, 0.2, 0.2)$, and $(-0.15, 0.11, 0.44)$, which correspond to the locations where the streamwise vortices are developing and quasi-developed, respectively. At both upstream locations, Q1 and Q4 contribute to local maxima of the total pressure, while Q2 and Q3 correspond to local minima, consistent with the trends observed at the AIP. At the $x/D_{AIP} = -0.78$ location, the Q1 and Q3 events contribute favorably to the local maxima and minima instances of total pressure, whereas Q2 and Q4 events act as negative contributors. Note, however, that this behavior is limited to the extrema, while overall Q2 and Q4 events dominate and contribute favorably to the total Reynolds stress. This indicates that, during the initial spatial growth of the vortices, the inward and outward bursts serve as primary sources of azimuthal distortion. At $x/D_{AIP} = -0.15$, where the vortices are quasi-developed, as illustrated in Figure (d–f), the trends observed in the conditional quadrant analysis mirror those at the AIP (Figure 6): ejection events enhance azimuthal distortion, while sweep events facilitate pressure recovery. This is unsurprising, as the vortices are elongated in the streamwise direction

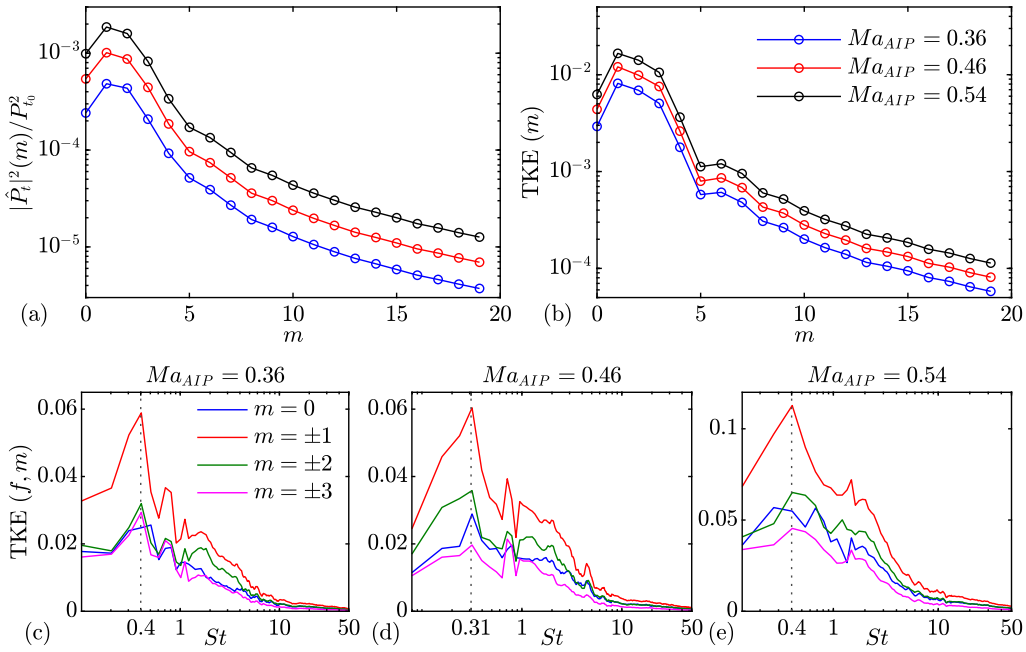


FIGURE 8. (a) Intensity of pressure fluctuations versus azimuthal wavenumber $m$ at probe 3. (b) Turbulent kinetic energy (TKE) versus $m$ at probe 3. TKE spectra as a function of Strouhal number $St$ for the most energetic azimuthal modes ($m = 0, \pm1, \pm2, \pm3$): (c) $Ma_{\mathrm{AIP}} = 0.36$, (d) $Ma_{\mathrm{AIP}} = 0.46$ and (e) $Ma_{\mathrm{AIP}} = 0.54$.

(Burrows *et al.* 2021), resulting in a higher correlation between $x/D_{AIP} = -0.15$ and AIP than $x/D_{AIP} = -0.78$ and AIP.

Finally, we examine the azimuthal wavenumbers and temporal frequencies associated with the distortion. To this end, all flow quantities along the third ring from the center, as shown in Figure 6(a), are interpolated from 8 to 128 points at each time instant using cubic spline interpolation, followed by a Fourier transform in the azimuthal direction. Figure 8(a) presents the intensity of pressure fluctuations and turbulent kinetic energy (TKE), obtained from the azimuthal Fourier transform averaged over time. Here, the TKE is normalized by the square of the speed of sound. Both spectra reveal that the four most significant azimuthal wavenumbers are $m = 1$, $m = 2$, $m = 3$ and $m = 0$, with $m = 1$ being the dominant mode. The prominence of $m = 1$ is expected and confirms that the counter-rotating vortices are the primary contributors to azimuthal flow distortion. The results shown here correspond to the third ring, though similar trends are observed for the other rings. Figure 8(c–e) shows the TKE for the four most energetic azimuthal wavenumbers as a function of Strouhal frequency, $St = fD/c_\infty M_{AIP}$. The temporal spectra are computed using Welch's method (Welch 2003) and subsequently averaged to improve statistical convergence. Across all cases, the $m = \pm1$ modes are the most energetic, followed by $m = \pm2$. For all $m$ and Mach numbers ($Ma_{\mathrm{AIP}} = 0.36, 0.46, 0.54$), the spectra peak at low frequencies ($St = 0.4$, 0.31, 0.4, respectively), indicating that the flow within the diffuser is dominated by large timescales and exhibits quasi-steady behavior.

The spatial field of TKE reconstructed using the $m = 0$ and $\pm1$ modes and averaged over time is shown in Figure 9. The $m = 0$ mode is included as it represents the

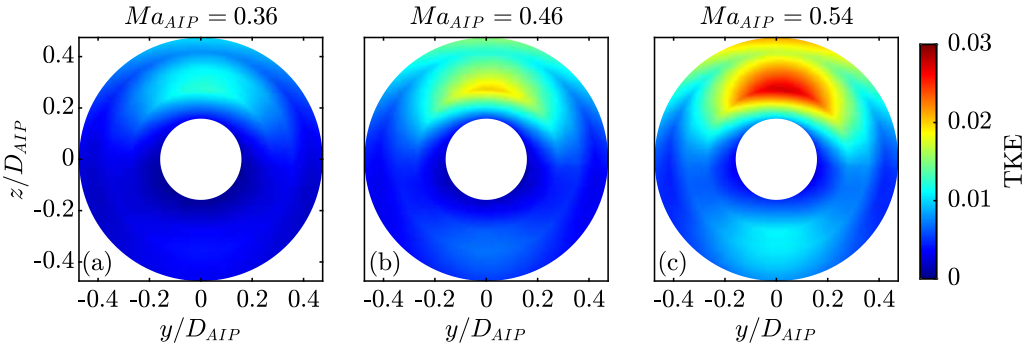


FIGURE 9. TKE fields reconstructed using $m = 0$ and $m = \pm 1$ azimuthal wavenumbers: (a) $Ma_{AIP} = 0.36$, (b) $Ma_{AIP} = 0.46$ and (c) $Ma_{AIP} = 0.54$

axisymmetric component, providing a more complete depiction of the flow field. For all three Mach numbers, the reconstructed TKE is concentrated near the upper wall, coinciding with regions of reduced pressure recovery. Note that these TKE fields were interpolated from the 40-probe rake and therefore do not precisely capture the spatial structure; they are presented here primarily for qualitative interpretation. Nevertheless, the reconstructed TKE fields reiterate that the $m = \pm 1$ wavenumbers associated with the counter-rotating streamwise vortices play a significant role in the azimuthal flow distortion.

## 4. Conclusions

This study investigates the development of streamwise vortices in a serpentine duct (SD-2) and their subsequent influence on flow distortion and pressure recovery loss at three Mach numbers, $Ma_{\mathrm{AIP}} = 0.36, 0.46$ and $0.54$. The adverse pressure gradient and centrifugal forces generated by the two bends of the duct induce flow separation, which produces a pair of counter-rotating Görtler vortices. As the flow evolves downstream, these vortices are advected from the periphery toward the duct centerline along the spanwise direction. The Görtler vortices eject low-momentum fluid from near the wall into the core, leading to azimuthal distortion and a loss of pressure recovery. This phenomenon is observed consistently across all three Mach numbers considered in this work. The vortices formed near the top wall are stronger than those near the bottom wall, causing greater total pressure loss in the upper region of the duct. Analysis of the joint PDFs of the streamwise and vertical velocity fluctuations reveals elliptically shaped distributions along the direction of ejection and sweep events. Near the onset of the counter-rotating vortices, ejection events are statistically more prevalent, whereas farther downstream, closer to the AIP where the vortices are fully developed, sweep events become dominant. A conditional quadrant analysis performed at the AIP shows that ejection events correspond to time instances of maximum total pressure loss, driving azimuthal distortion, while sweep events correspond to instances of minimum loss, attenuating the distortion. Spectral analysis further confirms that the azimuthal wavenumber $m = \pm 1$, associated with the counter-rotating vortices, carries the highest TKE, and the reconstructed TKE fields align with regions of pressure loss, highlighting the contribution of these vortices to azimuthal distortion.

**Acknowledgments**

The support of ONR to CTR under grant N000142312833 is gratefully acknowledged. This work was also supported by Boeing Research and Technology under grant #2024-UI-PA-100. This research used resources of the Oak Ridge Leadership Computing Facility, which is a DOE Office of Science User Facility supported under Contract DE-AC05-00OR22725. The authors acknowledge fruitful discussions with Dr. Chad Winkler from The Boeing Company.

## REFERENCES

Agrawal, R., Bose, S. & Moin, P. 2024*a* Nonequilibrium wall model for large eddy simulations of complex flows exhibiting turbulent smooth body separation. *Phys. Rev. Fluids* **9**, 124603.

Agrawal, R., Bose, S. & Moin, P. 2024*b* Reynolds-number-dependence of length scales governing turbulent-flow separation in wall-modeled large eddy simulation. *AIAA J.* **62**, 3686–3699.

Agrawal, R., Bose, S., Moin, P. & Winkler, C. M. 2025 Predictions of flow distortions inside a serpentine diffuser from large-eddy simulations. *AIAA Paper* 2025–3789.

Agrawal, R., Whitmore, M., Griffin, K., Bose, S. & Moin, P. 2022 Non-Boussinesq subgrid-scale model with dynamic tensorial coefficients. *Phys. Rev. Fluids* **7**, 074602.

Brear, M., Warfield, Z., Mangus, Z., Braddom, S., Paduano, J. & Philhower, J. 2004 Flow separation within the engine inlet of an uninhabited combat air vehicle (UCAV). *J. Fluids Eng.* **126**, 266–272.

Brès, G. A., Jordan, P., Jaunet, V., Le Rallic, M., Cavalieri, A. V. G., Towne, A., Lele, S. K., Colonius, T. & Schmidt, O. T. 2018 Importance of the nozzle-exit boundary-layer state in subsonic turbulent jets. *J. Fluid Mech.* **851**, 83–124.

Burrows, T., Vukasinovic, B., Glezer, A., Lakebrink, M. & Mani, M. 2021 Experimental and numerical investigation of active flow control of a serpentine diffuser. *AIAA J.* **59**, 607–620.

Cabot, W. & Moin, P. 2000 Approximate wall boundary conditions in the large-eddy simulation of high Reynolds number flow. *Flow Turbul. Combust.* **63**, 269–291.

Corino, E. R. & Brodkey, R. S. 1969 A visual investigation of the wall region in turbulent flow. *J. Fluid Mech.* **37**, 1–30.

Dean, W. 1927 Note on the motion of fluid in a curved pipe. *Phil. Mag.* **4**, 208–223.

Dean, W. 1928 The stream-line motion of fluid in a curved pipe. *Phil. Mag.* **5**, 673–695.

Goc, K., Moin, P., Bose, S. & Clark, A. 2023 Wind tunnel and grid resolution effects in large-eddy simulations of the high-lift common research model. *J. Aircr.* **61**, 267–279.

Harrison, N. A., Anderson, J., Fleming, J. L. & Ng, W. 2013 Active flow control of a boundary layer-ingesting serpentine inlet diffuser. *J. Aircr.* **50**, 262–271.

Huang, H., Lin, Z., Tan, H., Bai, M., Jia, M., Zhu, Y. & Liu, L. 2024 On the large-scale vortices in an L/D= 2.30 serpentine diffuser with internal bump. *Phys. Fluids* **36**, 116133.

Lakebrink, M. & Mani, M. 2018 Numerical investigation of dynamic distortion and flow control in a serpentine diffuser. *AIAA Paper* 2018–1283.

Lakebrink, M., Mani, M., Rolfe, E., Spyropoulos, J., Philips, D., Bose, S. & Mace, J. 2019 Toward improved turbulence-modeling techniques for internal-flow applications. *AIAA Paper* 2019–3703.

MacManus, D., Chiereghin, N., Prieto, D. & Zachos, P. 2017 Complex aero-engine intake ducts and dynamic distortion. *AIAA J.* **55**, 2395–2409.

Moin, P., Squires, K., Cabot, W. & Lee, S. 1991 A dynamic subgrid-scale model for compressible turbulence and scalar transport. *Phys. Fluids* **3**, 2746–2757.

Ng, Y., Luo, S., Lim, T. & Ho, Q. 2008 On the relation between centrifugal force and radial pressure gradient in flow inside curved and S-shaped ducts. *Phys. Fluids* **20**, 055109.

Stahl, S., Gaitonde, D., Powers, R. & Spyropoulos, J. 2023 Modal analysis of serpentine diffuser distortion. *AIAA Paper* 2023–3308.

Stratton, Z., Spyropoulos, J., Mani, M., Mace, J., Li, S., Fletcher, J., Vukasinovic, B. & Glezer, A. 2025 Development of an aggressive offset diffuser testbed with adaptive design characteristics. *AIAA paper* 2025–2108.

Triantafyllou, T., Nikolaidis, T., Diakostefanis, M. & Pilidis, P. 2015 Total pressure distortion levels at the aerodynamic interface plane of a military aircraft. *Aeronaut. J.* **119**, 1147–1166.

Wallace, J. M., Eckelmann, H. & Brodkey, R. S. 1972 The wall region in turbulent shear flow. *J. Fluid Mech.* **54**, 39–48.

Welch, P. 2003 The use of fast Fourier transform for the estimation of power spectra: A method based on time averaging over short, modified periodograms. *IEEE Trans. Audio Electroacoust.* **15**, 70–73.

Wenzel, L. & Blaha, R. 1977 Analysis of dynamic inlet distortion applied to a parallel compressor model. *Tech. Rep.,* NASA-TM-X-3522.

Winkler, C. & Davis, Z. 2017 Summary of the 3rd propulsion aerodynamics workshop: S-duct results. *AIAA Paper* 2017–4912.

Zachos, P., MacManus, D., Prieto, D. & Chiereghin, N. 2016 Flow distortion measurements in convoluted aeroengine intakes. *AIAA J.* **54**, 2819–2832.